

Multidomain Two-Phase Flow Model to Study the Impacts of Hydraulic Fracturing on Shale Gas Production

Guanglei Cui, Yuling Tan,* Tianyu Chen,* Xia-Ting Feng, Derek Elsworth, Zhejun Pan, and Chunguang Wang

 Cite This: *Energy Fuels* 2020, 34, 4273–4288

 Read Online

ACCESS |

 Metrics & More

 Article Recommendations

ABSTRACT: Hydraulic fracturing enhances the recovery of gas from ultralow permeability shales, into which water-based fracturing fluids, proppants, and activators are typically injected. However, the impacts of the existing complex multidomain response of a heterogeneous mineral and organic matrix and fractures on the resulting heterogeneity of reservoir transport properties caused by the hydraulic fracturing remain poorly understood. To address this defect, a multidomain multiphysics model is constructed to represent a two-phase flow within a three-component heterogeneous solid system (mineral and organic matrix and fractures) representing the functional complexity of the medium. This model partitions the shale reservoir into a stimulated reservoir volume (SRV) enclosed within an unstimulated reservoir volume (USRV). Different from the previous work, the shape of the SRV is treated as the spheroid instead of the rectangular shape and the size can be determined from the spatial distribution of microseismic events rather than artificially assumed. A two-phase flow model is established for both regions with the impacts of the effective stress variation on the fracture permeability considered and solved with a finite element formalism. The fidelity of the model is first verified using two field data sets from the Barnett and Marcellus shales with good fits achieved against time histories of production. Numerical studies then investigate the impacts of relevant parameters on shale gas production behavior; specially, the impacts of the effective stress and the existence of proppants are first reported. The variations in relative permeability and intrinsic permeability within the SRV are shown to dominate the early-time response of the gas flow rate. The long-term response is mainly dependent on the mass supply from the matrix system and the encapsulating USRV region. The effectiveness of hydraulic fracturing optimized as the SRV region is maximally extended in the horizontal direction and where the increase in permeability is a convex function against a concave function. The distal transport and placement of the proppant remarkably enhance the gas production rate and resist its decline as a result of the evolving high formation stress developed by pressure drawdown. For the selection of proppant type and placement, the resulting permeability and compressibility are of complementary importance as the first controls the initial gas flow rate, whereas the second determines the permeability trend with time. Proppant permeability decreases near-linearly for a constant compressibility but exponentially where compressibility is updated to represent the true response of the proppant pack. The proposed model applies a new approach for optimizing the hydraulic fracturing process and for analyzing the shale gas production behavior.

1. INTRODUCTION

The successful development of hydraulic fracturing (HF) makes the economic production of shale gas reservoirs feasible. The purpose of the HF is to create an extensive fracture network to enhance reservoir permeability.¹ However, as a consequence of water injection, the resulting reservoir damage may impair gas flow by processes such as water blocking.² The principal aim of this study is to investigate and quantify the impact of key HF-relevant parameters such as non-Darcy effects, water saturation, the form and distribution of the proppant pack, enhanced permeability, and evolution of pressure-drawdown-related effective stress on the resulting gas flow and recovery characteristics.

To calibrate the effectiveness of HF, the microseismic (MS) event distribution may be used to monitor fracture propagation³ and interpret the evolution of reactivated natural and artificial hydraulic fracture networks. A geomechanically based methodology is usually applied to the description of the

hydraulic fracture⁴ in which naturally occurring fractures are first located and hydraulic fracture propagation later simulated.^{5,6} For the analysis of gas production, discrete fracture network (DFN) models provide a feasible way to incorporate the hydraulic fracture network into the simulation of shale gas reservoirs.^{7,8} In DFN models, the hydraulic fractures are directly modeled and the computing nodes denote either the matrix system or the fracture system. When applied to reservoir simulations, the DFN approach exhibits three major defects: (1) the DFN is of limited fidelity as the MS signals are always contaminated by noise;⁹ (2) DFN

Received: January 6, 2020

Revised: February 25, 2020

Published: February 25, 2020



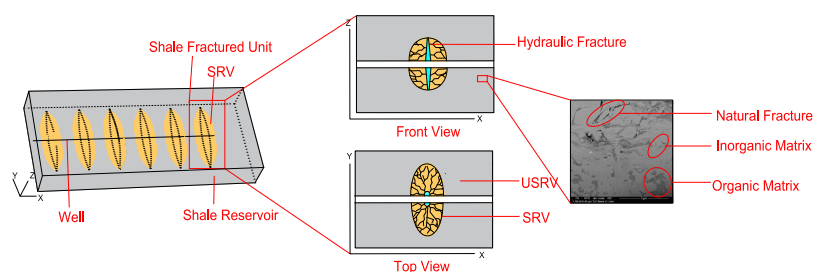


Figure 1. Geometry illustration of the multiphysics multidomain model (SEM image from Ambrose et al.⁴⁰).

approaches are usually highly time-consuming and computationally intensive;¹⁰ and (3) a significant amount of MS field data are required, but are rarely available in most the shale gas fields.¹¹

As an alternative method, equivalent continuum approaches have been proposed.^{12,13} In this approach, the shale reservoir is divided into a stimulated reservoir volume (SRV) and unstimulated reservoir volume (USRV).^{12,13} The SRV is defined as the region with conductive fractures,¹ whereas the USRV comprises the remainder of the original reservoir. Clearly, the shale gas production behavior strongly correlates with the SRV.^{12,14} The associated models are proposed based on the concept of the SRV. The analytical models for single gas flow were first proposed based on linear flow assumption.¹⁵ During the development of these models, the effects of gas in hydraulic fractures,¹⁶ secondary fractures,¹⁷ and the gas flow heterogeneous in the different regions¹⁸ are considered successively. However, these single-phase models are insufficient and their prediction accuracy was not good as the flowback is multiphase flow most of the time.¹⁹

During the HF process, a massive volume of water is injected into each well. Field data show a large proportion of that water is retained within the reservoir and that only 10–50% of the fracturing water flows back.²⁰ The presence and persistence of the retained water poses a threat to the productivity of the wells and the performance of the reservoir. Increasing the water phase saturation will occupy the gas flow channels and may lead to >70% reduction in the gas relative permeability of shales.^{21,22} Several analytical/semianalytical solutions have been obtained for the two-phase flow after some simplifications. Through these approaches, the impacts of fracture half-length and permeability,²³ fracture conductivity,²⁴ and fracture network complexity²⁵ were investigated. The formulations of analytical/semianalytical solutions are simple, and the interpretation procedures are convenient for industry use.²⁶ However, the vagaries of the gas/solid coupling process and complex water-gas flow behavior are typically ignored—because of the difficulty in the rigorous theoretical solution process.²⁷ Further, the complex flow behavior in organic matter, inorganic matrix, and hydraulic fractures are not consistently described²⁸ and the simple bi-wing fracture (planar fracture) is used to represent the complex hydraulic fracture network in most models.²⁶ To counter this, numerical approaches are widely applied to solve the complex coupling equations.^{28–30} In these models, the characteristics of multiporosity media³¹ and the coupling process between flow and stress field³⁰ are considered. However, in previous studies, the form of the SRV is typically artificially constrained to conform to a regular rectangle—representing an idealized hydraulic fracture or represented as a discrete-fracture mode fracture network stimulated system. These two approaches are far from

real field. In actuality, the approximate size and shape of the SRV are typically available from the spreading MS cloud of events. An ellipsoidal SRV can be assumed based on the field observations,^{9,32} together with numerical simulations.^{33,34} The evolution of permeability and diffusivity is also related to the spatiotemporal distribution of MS events^{3,35} and can be estimated from the linear diffusion equation.³⁶

Concurrent with injection of the fracturing liquid, proppants are pumped into the shale reservoir to retain any gains in permeability and to ensure the stable performance of wells and the optimal design of HF. Proppants can significantly enhance the permeability of shale reservoirs^{37,38} with its efficiency metered by proppant type, proppant arrangement,^{37,38} and stresses.³⁹ In addition to these two factors, gas flow is also affected by the non-Darcy effect²⁹ caused by the high permeability in the SRV region and the impact of the high effective stress³⁹ depending on the reservoir depth and reservoir pressure. A comprehensive and systematic study of the impacts of these relevant parameters on gas production, together with their sensitivities and interdependencies, has not been fully investigated, either theoretically or numerically.

As mentioned above, hydraulic-fracturing-induced reservoir heterogeneity and the impacts of the relevant parameters such as non-Darcy effects, water saturation, the form and distribution of proppants, enhancements in permeability, and the response of the reservoir to pressure-drawdown-induced stress remain poorly understood. This work addresses this knowledge gap through the development of a multidomain multiscale two-phase flow model to comprehensively examine the process of early-time HF through late-time reservoir production. The representation is necessarily multidomain as it contains both the SRV and the USRV, whose shape and size can be determined from the MS event—but also incorporates the constituted response of the reservoir as a three-component mixture comprising fractures separating mineral and organic matrix. Two field cases are adopted to verify the proposed model, followed by numerical simulations and sensitivity analyses to probe the effects of these parameters on shale gas production rates. The details are reported as follows.

2. MATHEMATICAL MODEL

After HF, the shale reservoir is effectively partitioned into an initial USRV and a SRV. In this section, a shale fractured unit is selected for illustration and it consists of both regions. A coordinate system is defined as the x -, y -, and z -axis along the well, dip, and vertical directions, respectively. As field observations of Patterson et al.³² and Yong et al.⁹ together with numerical simulations^{33,34} show, the SRV shape can be simplified as an ellipsoid. The longest axis is along the horizontal direction perpendicular to the well direction (y -

direction). The other axes are along the vertical direction (z -direction) and the well direction (x -direction), respectively. The illustration of shale fractured unit and SRV is shown in Figure 1.

Comprising a fracture system, an inorganic matrix system, and an organic matrix system,⁴⁰ the shale reservoir exhibits high heterogeneous mineral constituents, see Figure 1. Because of the heterogeneous properties, gas flows in shale blocks involves multiple scales. In the case that production starts, gas flows appear in shale blocks in three procedures successively. In the first step, the water-gas two-phase flow in the fracture system is usually described as Darcy or non-Darcy flow depending on the flow velocity.⁴¹ Then, free gas migrates from inorganic system to fracture system because of difference in gas pressure. In this process, the modified Darcy flow and the apparent permeability are applied owing to gas seepage effects.⁴² In the third step, declines of gas pressure lead to desorption of gas from adsorbed phases in organic matters to the free phase and diffuse into the inorganic pore system. The sequential flow and the corresponding governing equations are shown in Figure 2. In this work, we assume that the three

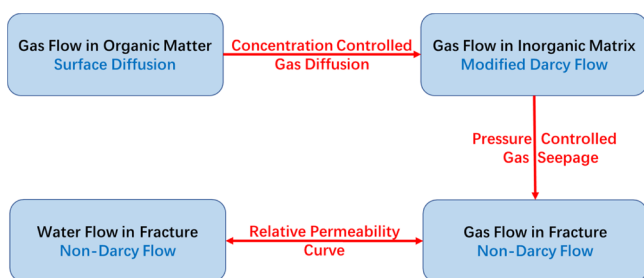


Figure 2. Interaction and relation of various porosity systems in the multidomain model (modified after Cao et al.,⁴⁴).

porosity systems exist in both the RSV and the URSV. The major difference is that the gas transport abilities are different in the two regions. In this work, we focused on the impacts of HF and its relevant factor on the shale gas production. These impacts are concentrated upon the fracture system. Therefore, two major assumptions are made (i) the effects of shale matrix deformation on the gas flow and the gas desorption which were well studied in our previous work⁴³ are ignored in this work; (ii) the impacts of matrix water on the gas production are not considered as the matrix water only takes up a small part because of the small pore throat of the shale matrix.⁴⁰ These assumptions were also adopted in the previous works.^{31,44}

2.1. Two-Phase Flow in the Fracture System. The conservation law for an immiscible two-phase flow in the fracture system is⁴⁵

$$\frac{\partial m_\alpha}{\partial t} + \nabla \cdot J_\alpha = Q_\alpha \quad (1)$$

in which m_α is the flow mass, Q_α is the flow source or sink, the subscript α represents water (w) and gas (g). The mass flux J_α of the fluid can be described as⁴⁵

$$J_\alpha = -\rho_\alpha \frac{k_f k_{ra}}{\mu_\alpha} \nabla p_a = -\rho_\alpha k_{ra} v_a \quad (2a)$$

$$v_a = \frac{k_f}{\mu_a} \nabla p_a \quad (2b)$$

in which k_f is the intrinsic permeability of the fracture system; k_{ra} refers to the relative permeability; μ_α denotes the viscosity; and p_a represents the pore pressure. v_a is the velocity vector which should be modified by the non-Darcy effect in the SRV region because of its larger permeability.⁴¹ In this work, the Forchheimer equation is applied to describe this non-Darcy effect as⁴¹

$$v_a = \frac{k_f}{\mu_a} \delta_a \nabla p_a \quad (3)$$

in which δ_a is a correction coefficient defined as

$$\delta_a = \frac{1}{1 + \frac{k_f}{\mu_a} \rho_a \beta_a |v_a|} \quad (4)$$

The parameter β_a is connected with the permeability of the porous media.⁴⁶ Based on Cooke's work,⁴⁷ the β_a factor could be expressed as a power law of permeability k_f as

$$\beta_a = \gamma k_f^\eta \quad (5)$$

in which γ and η are the reservoir-specific coefficients.

The water mass (m_{wf}) can be calculated as⁴⁸

$$m_{wf} = S_{wf} \rho_{wf} \phi_f \quad (6)$$

in which S_{wf} represents water saturation in the fracture system, ρ_{wf} denotes the water density, and ϕ_f symbolizes the porosity for the fracture system.

Gas in the fracture system (m_{gf}) consists of the free gas and the mass sources supplied by the inorganic matrix system

$$m_{gf} = S_{gf} \rho_{gf} \phi_f + Q_{in2f} \quad (7)$$

in which S_{gf} and ρ_{gf} refer to gas saturation and gas density in the fracture system, separately.

The gas mass transfer (Q_{in2f}) is in the term of gas seepage and controlled by the gas pressure difference between the fracture and the inorganic matrix systems⁴²

$$Q_{in2f} = \frac{\chi_{in} k_{apin}}{\mu} \rho_{in} (p_{gf} - p_{in}) \frac{M}{RT} \quad (8)$$

where χ_{in} denotes a shape factor, ρ_{in} represents the gas density in the fracture system, k_{apin} is the apparent permeability of the inorganic system, M denotes the molar weight of the molecule, R represents universal gas constant, and T denotes the reservoir temperature.

Therefore, the two-phase flows in fracture system are

$$\frac{\partial (S_{wf} \rho_{wf} \phi_f)}{\partial t} = \nabla \cdot (\rho_{wf} k_{rw} v_w) \quad (9a)$$

$$\frac{\partial (S_{wg} \rho_{wg} \phi_f)}{\partial t} = \nabla \cdot (\rho_{wg} k_{rg} v_g) - \frac{\sigma_{in} k_{apin}}{\mu} \rho_{in} (p_f - p_{in}) \quad (9b)$$

without supplementary formulas for capillary pressure and saturation, the four variables (S_{gf} , S_{wf} , p_{gf} , and p_w) cannot be solved^{45,49}

$$S_{wf} + S_{gf} = 1 \quad (10)$$

$$p_{cf} = p_{gf} - p_{wf} \quad (11)$$

where p_{cf} represents the capillary pressure in the fracture system. This study uses the Brooks and Corey formulation⁵⁰ for calculating the capillary pressure

$$p_{cf} = p_e (s_{ew})^{-1/\lambda} \quad (12)$$

where p_e refers to the entry pressure of the nonwetting phase, s_{ew} denotes the water-phase effective saturation, and λ represents the parameter associated with the distribution of pore sizes. This study assumes λ being equivalent to 2. The definition of effective water saturation is shown as follows⁴⁵

$$s_{ew} = \frac{S_{wg} - S_{wr}}{1 - s_{wr} - s_{gr}} \quad (13)$$

where s_{wr} and s_{gr} refer to saturations of irreducible water and residual gas of the fractures.

In this study, the functions below are used for controlling relative permeability, as described by Leverett⁵¹

$$k_{rg} = (1 - s_{ew})^2 (1 - s_{ew}^2) \quad (14)$$

$$k_{rw} = \sqrt{s_{ew}} (1 - (1 - s_{ew}^{1/m})^m)^2 \quad (15)$$

where k_{rg} and k_{rw} separately denote the relative permeabilities of gas and water, and m is the pore size distribution index,⁵² and this study assumes m being equivalent to 0.5.

2.2. Slip Flow in the Inorganic Matrix. Slip flow is adopted to describe the flow state in the inorganic matrix, whereas the mass conservation law is⁴²

$$\frac{\partial m_{in}}{\partial t} + \nabla \cdot J_{in} = Q_s + Q_{in2f} \quad (16)$$

where J_{in} , Q_s , and Q_{in2f} symbolize the mass flux for gas transport of inorganic minerals, a term of mass source, and mass transfer between the inorganic matrix and the fracture, respectively.

Gas mass content m_{in} contains free gas and the gas mass source applied by the organic system⁴²

$$m_{in} = \rho_{in} \phi_{in} + \rho_{ga} \rho_s m_{or} \quad (17)$$

where ρ_{in} denotes gas density in the inorganic system and ϕ_{in} represents the inorganic porosity; J_{in} symbolizes the mass flux expressed by a pressure gradient as an improved Darcy's equation

$$J_{in} = -\frac{k_{apin}}{\mu} \rho_{in} \nabla p_{in} \quad (18)$$

where k_{apin} represents the apparent permeability for the inorganic system⁴²

$$k_{apin} = \left(1 + \frac{4Kn_{in}}{1 + Kn_{in}} \right) k_{in} \quad (19)$$

2.3. Gas Diffusion in the Organic Matter. Diffusion time in the organic matter is taken to describe the transfer rate of the mass between the organic and the inorganic systems^{41,53}

$$\frac{dm_{or}}{dt} = -\frac{1}{\tau} [m_{or} - m_e(p_{wall})] \quad (20)$$

where $m_e(p_{wall})$ refers to the concentration of gas at the equilibrium state with interface pressure p_{wall} , in which diffusion time for the organic matter is

$$\tau = \frac{1}{\omega D} \quad (21)$$

where D (m²/s) and ω denote the diffusion coefficient of organic matters and a shape factor.

The diffusion in the organic matter is widely studied, and bulk flow, Knudsen flow,⁵⁴ transition flow, and their effective combinations⁴³ are mostly applied. The above categories are focused on free gas transportation. Whereas in the organic matter both the free and adsorption gas coexist, the latter term takes a bigger proportion.⁴³ In this work, we focused on the impacts of the HF and its relevant parameters on the gas production characteristic. The details of the impacts of the gas diffusion in the shale matrix on the gas production characteristic can be found in our previous work.⁴³ For simplicity, an assumption is made that only the adsorption gas is considered in the organic matter. Surface diffusion is widely applied to the description of adsorption gas transportation and the diffusion coefficient varies with the pressure as⁵⁵

$$\frac{D_s}{D_{s_0}} = \frac{1}{1 - \theta} \quad \text{and} \quad \theta = \frac{p}{p + P_L} \quad (22)$$

where P_L and θ represent the Langmuir pressure and the surface coverage for adsorption layers, respectively; D_s denotes the surface diffusion coefficient and D_{s_0} represents the surface diffusion coefficient at the initial state.

The study assumes the existence of a pseudo-steady state⁴¹ and equivalence of interface pressure p_{wall} with inorganic matrix pressure p_{in} . In such an approach, the gas pressure gradient and the stress gradient are not considered in both systems,⁴³ both systems are homogenized and at a pseudo-steady state. The adsorbed gas content in equilibrium $m_e(p_{wall})$ is calculated by the Langmuir isotherm

$$m_e(p_{wall}) = \frac{V_L p_{in}}{P_L + p_{in}} \quad (23)$$

2.4. Correlation between Shale Permeability and Effective Stress. The fracture compressibility is used to describe the stress sensitivity of the fracture permeability⁵⁶

$$k_f = k_{f0} e^{-3c_f(\sigma_e - \sigma_{e0})} \quad (24)$$

in which σ_e represents the effective stress; c_f refers to the fracture compressibility, with the following definition⁵⁶

$$c_f = -\frac{1}{\phi_f} \frac{\partial \phi_f}{\partial \sigma_e} \quad (25)$$

in which ϕ_f symbolizes the porosity for the fracture system. Difference of stress from pore pressure is taken to define the effective stress

$$\sigma_e = \sigma - \alpha p_f \quad (26)$$

in which α is Biot's coefficient. Different from previous work, pore pressure combines gas and water pressures for the fracture system (p_f)⁴⁵

$$p_f = S_{wf} p_{fw} + S_{gf} p_{fg} \quad (27)$$

and gas pressure for the inorganic system (p_{in})

$$p_{in} = p_g \quad (28)$$

3. MODEL VERIFICATION

3.1. Implementation of the Numerical Model. The coupled two-phase flow model described above is applied to

and computed using a commercially available solver of Partial differential equations (PDE), that is, COMSOL Multiphysics (Version 5.4). The difficulties of this work lie in the solution of the two-phase flow model as eq 8. The expanded form of eq 8 can be written as

$$\begin{aligned} & (\rho_{wf}\phi_f - \rho_{wf}\phi_f S_{wf} C_w dpc_sw) \frac{\partial(S_{wf})}{\partial t} + \rho_{wf}\phi_f S_{wf} C_w \frac{\partial(p_g)}{\partial t} \\ & + \nabla \left(-\rho_{wf} \frac{k_f k_{rw}}{\mu_w} \delta_w (\nabla p_g - dpc_sw \nabla S_{wf}) \right) \\ & + \rho_{wf} S_{wf} \frac{\partial(\phi_f)}{\partial t} \\ & = 0 \end{aligned} \quad (29a)$$

$$\begin{aligned} & \rho_{wg}\phi_f \frac{\partial(S_{wf})}{\partial t} + \rho_{gf}\phi_f S_{gf} C_g \frac{\partial(p_g)}{\partial t} + \nabla \left(-\rho_{wg} \frac{k_f k_{rg}}{\mu_g} \delta_a \nabla p_g \right) \\ & + \rho_{wg} S_{wg} \frac{\partial(\phi_f)}{\partial t} \\ & = -\frac{\sigma_{in} k_{apin}}{\mu} \rho_{in} (p_f - p_{in}) \end{aligned} \quad (29b)$$

in which the dpc_sw represents the partial differential of capillary pressure to the water saturation and can be expressed as⁴⁵

$$dpc_sw = p_e \left(-\frac{1}{\lambda} \right) (s_{ew})^{-1/\lambda-1} \quad (30)$$

The above equation takes compressibility of water and gas into account as well. That is to say, gas/water density changes with pore pressure, instead of a constant

$$\rho_\alpha = -1/C_\alpha (d\rho_\alpha/dp_\alpha) \quad (31)$$

in which C_α is the fluid compressibility and can be obtained from NIST (<https://webbook.nist.gov/chemistry/fluid/>).

Equation 29 serves as the last equation of the gas/water flow in the fracture system. The non-Darcy flow also brings the difficulties in the model simulation as the correction coefficient δ_α and velocity v_α are interrelated. To solve this, four subequations are needed to be solved simultaneously: three subequations for the velocity vector in the three directions (eq 2b) and one for eq 29b, instead of one for Darcy flow. In such an approach, the interrelated relationship can be solved through the iterations of the four subequations. To achieve the above goal, the General Form PDE Interface in the COMSOL with four variables (velocity v_α in the three directions and the liquid pressure) is selected. Meanwhile, the COMSOL Darcy module is taken to solve the slip flow of the inorganic matrix system (eq 16) and the gas diffusion in the organic matrix (eq 20) is achieved by the General Form PDE Interface. The relationship between permeability and effective stress (eq 24) is defined in variable definitions.

3.2. Model Buildup and History Matching of Barnett Shale. **3.2.1. Introduction of Well 314 in Barnett Shale.** To ensure the applicability, we employed the proposed model to historically match the gas production data. In this work, the data of two horizontal wells from Barnett Shale and Marcellus Shale,^{57,58} respectively, were used. First, the data collected from Well 314 in Barnett Shale is introduced. Barnett Shale is the primary source in the Paleozoic petroleum system in Fort

Worth Basin and among gas reservoirs of highest productivity across the US at present.⁵⁹ Well 314 is a horizontal well and subjected to multistage HF treatment, showing the initial pressure of 20.7 MPa in the reservoir and a constant bottom-hole pressure of 3.45 MPa. Production data for over 1600 days are available in a history match.

3.2.2. Model Buildup and History Match of Barnett Shale.

In the well 314, there are totally 28 hydraulic fractures with fracture spacing of only 30.5 m. As the distance between two hydraulic fractures is small, it is assumed that the ellipsoid-shaped SRV area induced by each hydraulic fracture is linked together. In the simulation model, the reservoir is set as a cuboid with a volume of 1000 m × 200 m × 120 m and the linked SRV is shaped like a cuboid with eight fillet angles. The geometry of the simulation model and SRV are illustrated in Figure 3.

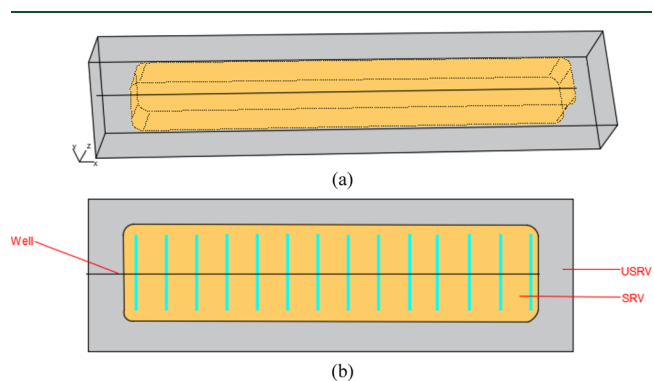


Figure 3. Geometry illustration of the simulation model for well 314 in Barnett shale; (a) 3D simulation model and (b) top view.

For the gas flow model in the fracture system, we apply constant bottom-hole pressure (3.45 MPa) to the well to simulate extraction pressure of hydraulically formed fractures, without flow boundary conditions at other boundaries. With regard to the gas flow model in organic and inorganic matrixes, no flow boundary conditions are used because of absence of direct contact with hydraulically formed fractures.⁴² Also, a constant water saturation is applied to the well as the water flow boundary with the value of 0.2. The reservoir information of Barnett shale are listed in Table 1. It should be noted that in the table the general parameters denote the parameters for the properties of gas and water; the shared parameters means the parameters that we assumed for the two-phase flow calculation which are the same for both reservoirs; the reservoir parameters were collected from Yu et al.,⁶⁰ and Cao et al.⁶¹ and they may not be the same with the previous work (in the same order) as the mathematical model is different.

Results of matched gas production rates as well as comparisons with our previous work⁴² and Cao' work⁴⁴ are illustrated in Figure 4. Also, the results of considering and without considering the non-Darcy effect are drawn. In our previous work, we assumed that organic system is embedded within the inorganic system in the shale matrix and both systems are dual-porosity media. The shale permeability is defined as a function of strains representing the stress transfer between fractures and the matrix without considering the water phase flow. In Cao' work, a multiscale-multiphase simulation model was proposed while the SRV region is artificially assumed as the rectangular shape. In our previous model, the initial gas production rates are larger than the field data

Table 1. Property Parameters of Barnett Shale^{60,61a}

general parameters	value	general parameters	value
gas density (kg/m ³)	0.714	gas viscosity (Pa·s)	2×10^{-5}
coefficient for relative permeability, m	0.5	coefficient for capillary pressure, λ	2
universal gas constant (J/(mol·K))	8.314	molar mass of methane (kg/mol)	0.016
compressibility of methane (Pa ⁻¹)	1.4×10^{-5}	compressibility of methane (Pa ⁻¹)	3.8×10^{-10}
Shared Parameters		Shared Parameters	
residual gas saturation	0.1	residual water saturation	0.05
coefficient for relative permeability, m	0.5	nonwetting phase entry pressure (MPa)	0.1
non-Darcy parameter (γ)	5×10^8	non-Darcy parameter (η)	-1.5
Reservoir Parameters		Reservoir Parameters	
reservoir temperature (°C)	65.6	bottom hole pressure (MPa)	3.45
fracture space (m)	30.5	initial gas pressure (Mpa)	20.7
size of simulation area (cube, m)	$1000 \times 200 \times 120$	size of USRV (cube, m)	$860 \times 100 \times 90$
fracture permeability in SRV, k_{fx} (m ²)	5×10^{-17}	fracture permeability in USRV, k_{fx} (m ²)	1×10^{-18}
k_{fy}/k_{fx}	0.8	k_{fz}/k_{fx}	0.2
inorganic permeability in SRV, k_{inx} (m ²)	2×10^{-18}	inorganic permeability in USRV, k_{inx} (m ²)	2×10^{-20}
k_{iny}/k_{inx}	0.9	k_{inz}/k_{inx}	0.1
fracture porosity in SRV	0.04	fracture porosity in USRV	0.01
inorganic porosity in SRV	0.02	inorganic porosity in USRV	0.005
fracture compressibility in SRV (MPa ⁻¹)	0.0047	shape factor in inorganic matrix (m ⁻²)	25
fracture compressibility in USRV (MPa ⁻¹)	0.02	bottom hole water saturation	0.1
surface diffusion coefficient (s)	4.5×10^9	Biot's coefficient	0.8
Initial water saturation in SRV	0.6	initial water saturation in USRV	0.2
Langmuir pressure constant (MPa)	4.48	Langmuir volume constant (m ³ /kg)	0.005

^aIn the table, the subscripts f and in represent the fracture and inorganic matrix system, and x, y, and z mean the permeability in the three directions. In this case, the fracture compressibilities are assumed equal in the three directions of both SRV and USRV regions as the detailed information of the proppant are not known in the previous work.

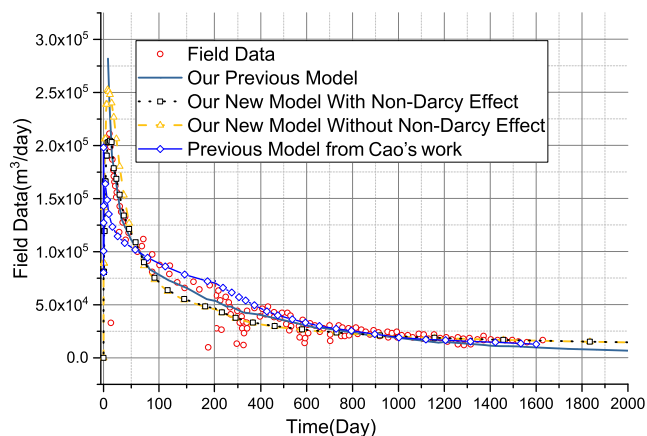


Figure 4. History match for field data collected from Barnett Shale.

because of ignorance of the impact of water saturation. In Cao's work,⁴⁴ the initial gas production rates are much smaller than the field data. However, the initial gas production rates obtained from the current model are closer to the field data. However, both the previous approaches can fit the production data during the 100–400 days compared with our new model. With the decreasing of the water saturation, both gas saturation and gas relative permeability increase. Consequently, long-term production rates of gas obtained from the current model are higher than that from the previous models and closer to the field data. We also find that the non-Darcy effect has a significant impact on the initial gas rate, whereas it has little impact on the long-term gas flow rate.

3.3. Model Buildup and History Match of Marcellus Shale. **3.3.1. Introduction of a Horizontal Well in Marcellus Shale.** As a kind of black sedimentary rock formed in Middle Devonian in the Appalachian Basin Province, Marcellus Shale has extremely poor permeability (0.1–0.00001 mD).⁶² Drilled

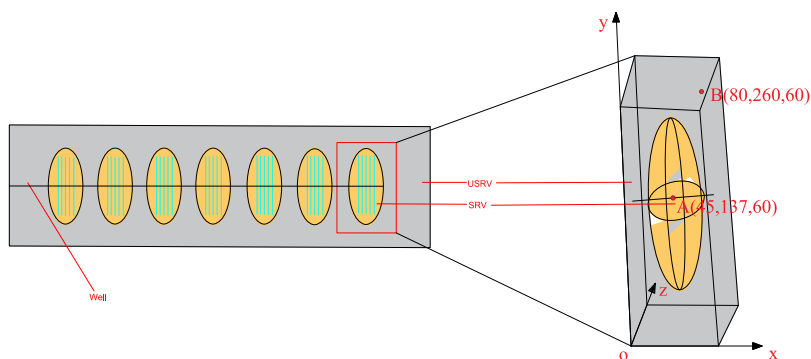


Figure 5. Geometry illustration of the multiphysics multidomain model.

to lower sections of Marcellus formation, the well was accomplished through fracturing with seven stages (each of which involved five perforation clusters) over 630 m in the lateral. It was designed for treatment where 450,000 gallons of slick water was used in each stage, with sand chosen as the proppant. Production data available for history match only lasted for 200 days.⁵⁸

3.3.2. Model Buildup and History Match of Marcellus Shale. The distance between different fracture stages is much larger than that between different perforation clusters in a specific stage.^{29,57} Based on that, a unit is selected containing a fracture stage (five perforation clusters) and its adjacent area. We assumed that the SRV area induced by each perforation cluster is linked together and forms a spheroid shape area. In the simulation model, the study area is set up as a cuboid with the volume of 92 m × 280 m × 120 m and semiaxis of the SRV area (spheroid shape) are separately 35, 100, and 50 m (in x , y , and z directions). Geometries of the reservoir and SRV are illustrated in Figure 5.

The mechanic and flow boundary conditions are similar to the case of Barnett Shale. Especially, we define a linear decline function to represent the variation of fracture permeability from the center of the SRV to the USRV area. The bottom hole pressure can be obtained from Meyer's work⁵⁸ (Figure 6).

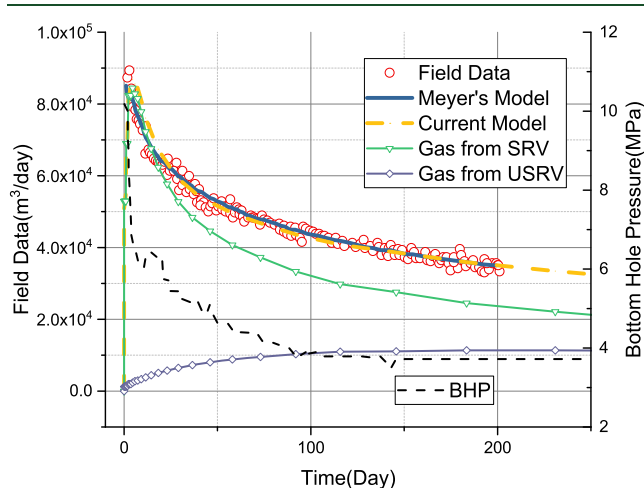


Figure 6. History match for field data collected from Marcellus Shale.

Reservoir information of Marcellus shale were collected from Yu and Sepehrnoori²⁹ and Yu et al.⁶⁰ and are listed in Table 2. The general and shared parameters are not listed in the table as they are the same and the fracture compressibility within SRV and USRV can be determined from our experiment work.^{37,63}

Results of matched gas production rates, together with comparisons with Meyer's model,⁵⁸ are illustrated in Figure 6. As observed in the figure, both models can match the field data perfectly. The gas contributions from the SRV and USRV are also illustrated. Obviously, most gases are from SRV whereas little gas comes from the USRV for a short time.

4. RESULTS AND DISCUSSION

In the previous section, field data collected from Barnett shale and Marcellus shale are adopted for verifying the proposed two-phase flow model. Two associated simulation models are established considering the different HF treatments of the two reservoirs. In this section, the variations of the non-Darcy effect, and both relative and intrinsic permeabilities are

investigated. Then, the simulation model of Marcellus Shale is selected as the benchmark model for more numerical analyses.

4.1. Variations of non-Darcy Effects and Relative and Intrinsic Permeability. The variations of the non-Darcy effect and both relative and intrinsic permeabilities during the gas production process are first investigated. The simulation model of Barnett Shale is selected for the variations of non-Darcy effects and the simulation model of Marcellus Shale is selected for the variations of relative and intrinsic permeabilities.

4.1.1. Variations of non-Darcy Effects. The variations of non-Darcy effect (δ_g) in both SRV and USRV regions are drawn in Figure 7 and also the direction dependences are illustrated.

Compared with the previous work,^{41,46} we find that the value of the non-Darcy effect (δ_g) in the shale reservoir is much smaller than that in the coal reservoir because of its smaller permeability. In the shale reservoir, the non-Darcy effect (δ_g) in the SRV region is bigger than that in the USRV region. For the direction dependency, the different laws are observed: the non-Darcy effect (δ_g) in the z direction is much larger than that in the x direction in the SRV region as the β factor (eq 4) is in inverse proportion to the velocity, whereas in the USRV region, the non-Darcy effect (δ_g) in the y direction is bigger than those in the x and z directions.

4.1.2. Variations of Relative and Intrinsic Permeabilities. To illustrate the variations of gas/water saturations and gas/water relative permeabilities, two representative points are selected, and the results are shown in Figure 8. Point A is in the center of the SRV and point B is in the USRV near the SRV region (the locations and coordinates are shown in Figure 5). As shown in the figure, the water saturation and relative permeabilities decline with production time, whereas the gas saturation and relative permeabilities increase with time. Point A in the SRV region has larger water saturation and relative permeabilities but with rapid decline. Conversely, point B in the USRV region has a larger gas saturation and relative permeabilities with a small variation.

Also, the evolutions of the intrinsic permeability of both points are illustrated in Figure 9 together with their direction dependences and gas pressures. As shown in the figures, the decline of gas pressure at point A is much quicker than that at point B. However, the permeability decreasing of point A is much smaller than that of point B because of the proppant support. For the direction dependency, the permeability decline in the x direction is much smaller than those in y and z directions because of its smaller fracture compressibility value as shown in Table 2.

4.2. Impacts of the Water Saturation-Influenced Relative Permeability. In the following section, the impacts of the relative permeability, intrinsic permeability, SRV size, proppants, and effective stress are investigated. The simulation model of Marcellus Shale is selected as the benchmark model for these numerical analyses.

As mentioned above, the reservoir is injected with slick water which serves as the fracturing liquid. Because of ultrasmall pore throats and water-adsorption of clay minerals in the shale matrix, a majority of water stays in the reservoir occupying the channel for gas flow. This section studies the impacts of water retention amount on production of shale gas and the results are given in Figure 10. Figure 10a illustrates that the water saturation significantly affects the early time

Table 2. Property Parameters of Marcellus Shale^{29,60a}

reservoir parameters	value	reservoir parameters	value
reservoir temperature (°C)	79.4	bottom hole pressure (MP _a)	Figure 6
fracturing cluster space (m)	92	initial gas pressure (Mpa)	32.6
size of simulation area (rectangle, m)	92 × 280 × 120	size of SRV (spheroid, m)	30 × 100 × 50
fracture permeability in SRV, k_{fx} (m ²)	5×10^{-16}	fracture permeability in USRV, k_{fx} (m ²)	1×10^{-18}
k_{fy}/k_{fx}	1.2	k_{fz}/k_{fx}	0.05
inorganic permeability in SRV, k_{inx} (m ²)	5×10^{-18}	inorganic permeability in USRV, k_{inx} (m ²)	8×10^{-20}
k_{iny}/k_{inx}	0.8	k_{inz}/k_{inx}	0.05
fracture porosity in SRV	0.08	fracture porosity in USRV	0.04
inorganic porosity in SRV	0.06	inorganic porosity in USRV	0.015
shape factor in inorganic matrix (m ⁻²)	25	surface diffusion coefficient (s)	6×10^9
C_{fx} in SRV (MPa ⁻¹)	0.0051	C_{fy} in SRV (MPa ⁻¹)	0.0080
C_{fz} in SRV (MPa ⁻¹)	0.0060	C_{fx} in USRV (MPa ⁻¹)	0.018
C_{fy} in USRV (MPa ⁻¹)	0.021	C_{fz} in USRV (MPa ⁻¹)	0.031
initial water saturation in SRV	0.5	initial water saturation in USRV	0.1
Langmuir pressure constant (MPa)	4	Langmuir volume constant (m ³ /kg)	0.003
bottom hole water saturation	0.1	Biot's coefficient	0.8

^aIn the table, the subscript f represents the fracture system, and x, y, and z mean the variables in the three directions.

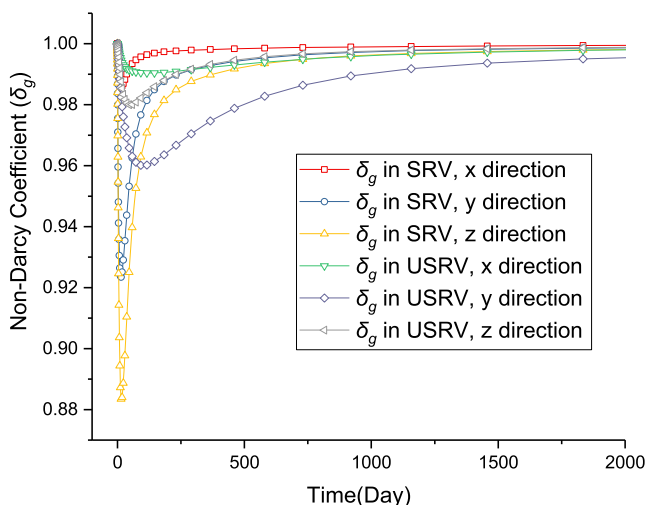


Figure 7. Variation of the non-Darcy effect (δ_g).

production behavior of gas, with higher water saturation leading to lower gas production rate and less total gas amount.

As to long-time gas production behavior, the water saturation has little impact as shown in Figure 10b.

To explore the reason, we also illustrate the variations of water and gas saturations and relative permeabilities (Figure 11) and here the average value of SRV is used. Water saturation and relative permeability both decrease, conversely gas saturation and relative permeability increase during the gas depletion process. Comparing Figures 10 and 11, we find that the differences in gas relative permeability between varied water saturations are large, whereas there are little differences in production rate, particularly in long-term production. In other words, water saturation and relative permeability only affects early time production behavior and has little impact on long-term production behavior. As our previous work determined,⁴² the long-time production behavior is mainly dependent on the mass supply source from the matrix system.

4.3. Impacts of the Enhanced Intrinsic Permeability.

The HF would enhance the intrinsic permeability by creating new fractures and extending natural fractures. The enhanced intrinsic permeability value and its distribution in the SRV are the critical factors for evaluating the efficiency of HF. This

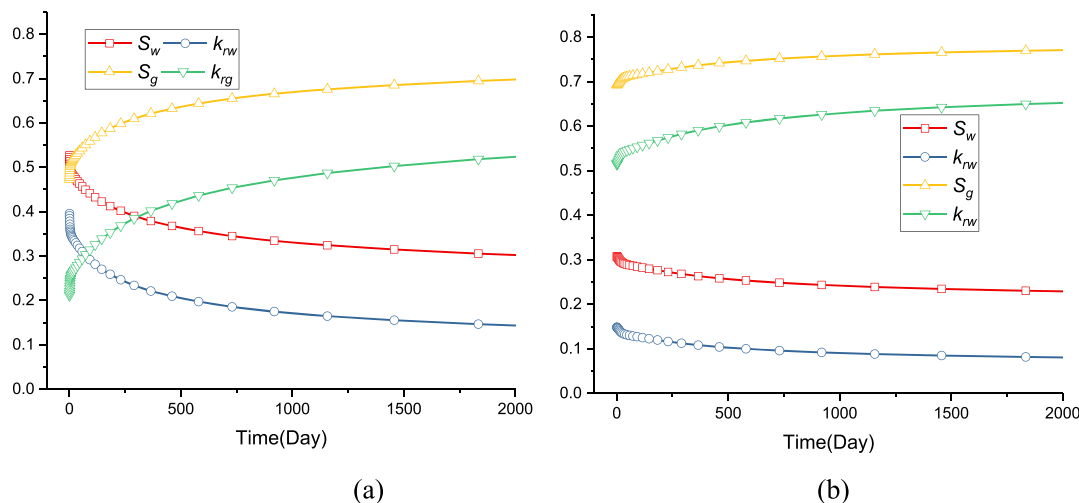


Figure 8. Gas/water saturations and gas/water relative permeabilities of (a) point A in the center of SRV and (b) point B in the USRV.

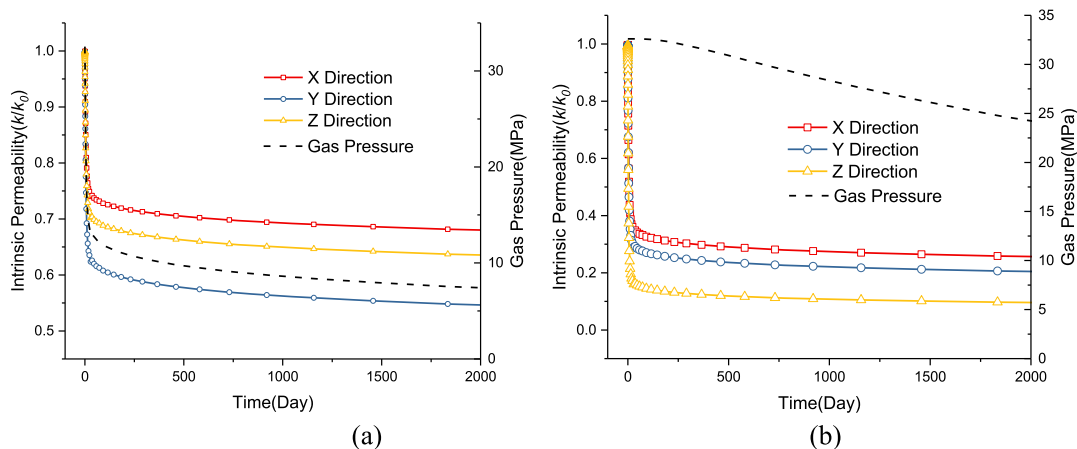


Figure 9. Evolution of intrinsic fracture permeability (a) point A in the center of the SRV and (b) point B in the USRV.

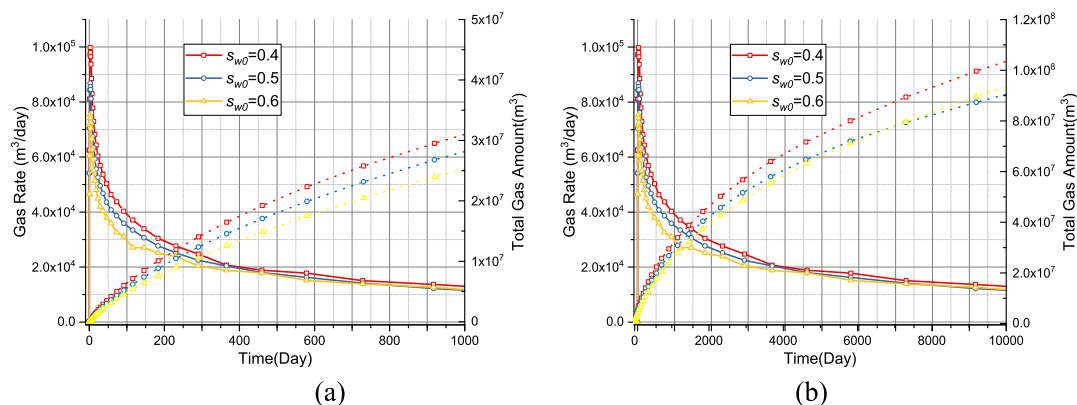


Figure 10. Effects of water saturation upon the production behavior of shale gas in a (a) short term and (b) long term.

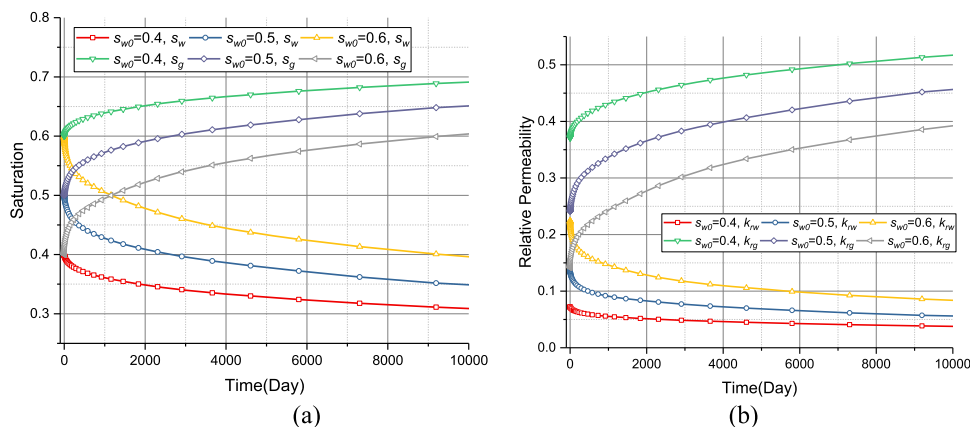


Figure 11. Evolutions of (a) water and gas saturation and (b) water and gas relative permeability.

section probes the effects of these two factors on the gas production process.

4.3.1. Impacts of Enhanced Intrinsic Permeability Value.

The impacts of the enhanced intrinsic permeability value are first investigated. This section only studies the effects of the biggest value and permeability distribution is kept the same. Figure 12 depicts the results. The permeability value exerts significant effects on early time production behaviors, whereas it imposes a slight impact on long-term ones especially for gas rate after 4000 days. A similar conclusion can be obtained that the long-time ones are basically dependent on the gas source

supply from the matrix system rather than the flowability of the fracture system.

In the above investigation, the permeabilities in three directions are enhanced or decreased at the same ratio. Also, the sensitivity of permeability value in each direction to the shale gas production is investigated, with results given in Figure 13. It can be observed from the figure that, the shale production process is most sensitive to the permeability value in the y-direction as it brings the largest or smallest gas rate when the permeability values are enhanced or decreased at the same ratio.

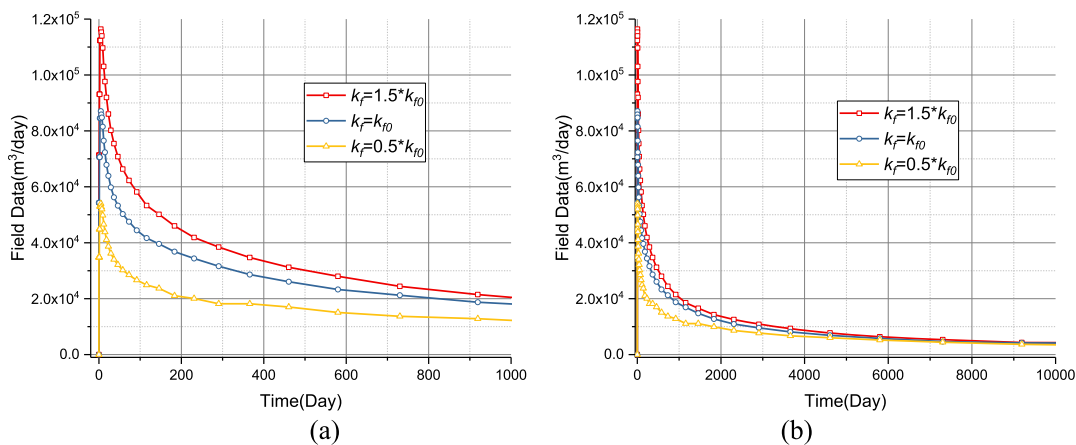


Figure 12. Impact of the enhanced permeability value on the gas production behavior (a) short-term and (b) long-term.

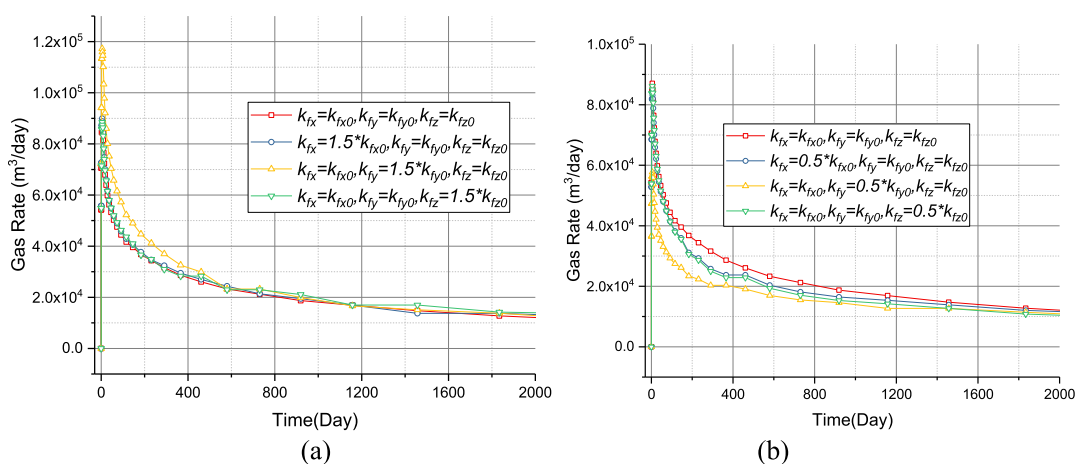


Figure 13. Production rate with (a) increased permeability and (b) decreased permeability. x , y , and z represent the values of the x -, y -, and z -axes, separately.

4.3.2. Impacts of Enhanced Intrinsic Permeability Distribution. In the previous work, the enhanced intrinsic permeability is linearly decreased from the center of the SRV region to its edge. In this section, we designed the other three paths from its maximum value to its initial value. One is the concave function below the linear function, the second is the convex function above the linear function, and the last term is the uniform distribution where the geometric average value is used. The convex distribution represents the field case where the complex fracture network can be formed at the jet hole and propagate in all directions. Conversely, the concave distribution represents the case where the complex fracture network can only extend within a certain range and rapidly disappear. The illustration of the four-distribution profile is illustrated in Figure 14. The results are illustrated in Figure 15.

As shown in Figure 15a, the enhanced permeability distribution has a significant impact on short-time production behavior. The convex function brings the largest gas rate, followed by the linear distribution, uniform distribution, and concave function distribution. To achieve the convex distribution in the field practice, not only the complexed fracture network is required but also it should extend as far as possible in three directions. As shown in the experiment^{64,65} and simulation work,⁶⁶ tortuosity of a main crack and the average number of cracks increased with the decrease in fluid viscosity. HF using low-viscosity fluid tends to generate and

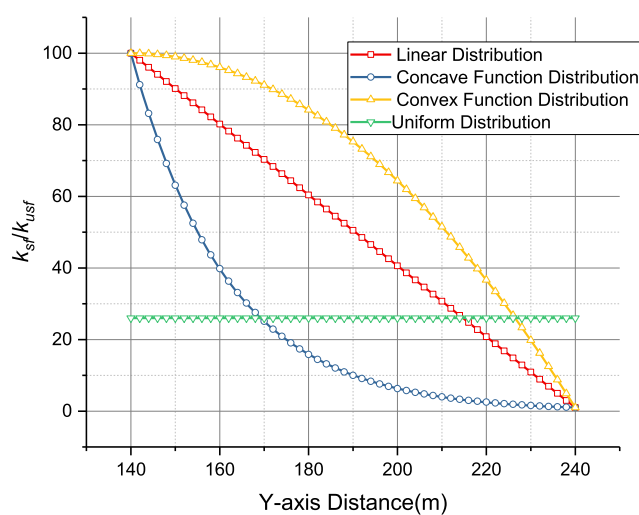


Figure 14. Illustration of the four-permeability-distribution scenarios taking the Y-axis of a spheroid as an example.

induce extensive three-dimensional cracking rather than the two-dimensional cracking observed for the high-viscosity fluid. However, the differences between different permeability distributions are lessened with the gas production process, as

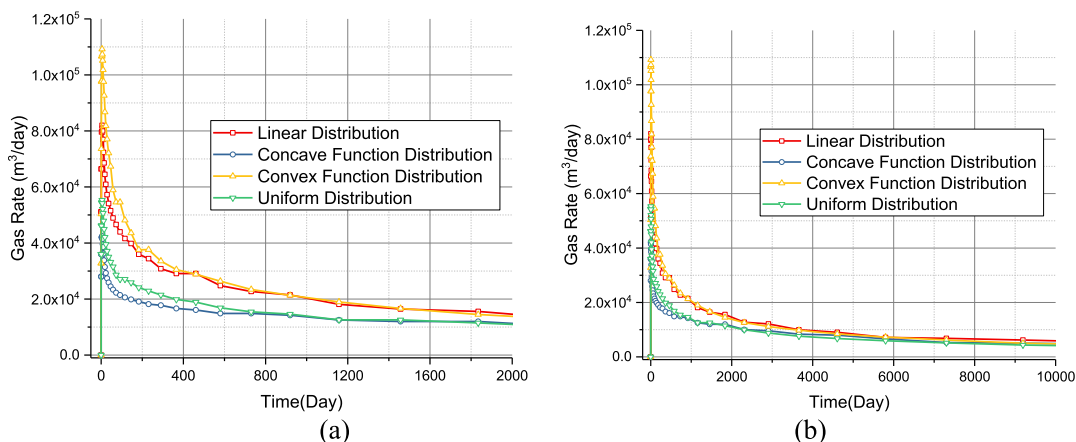


Figure 15. Impact of the enhanced permeability distribution on the gas production behavior (a) short-term and (b) long-term.

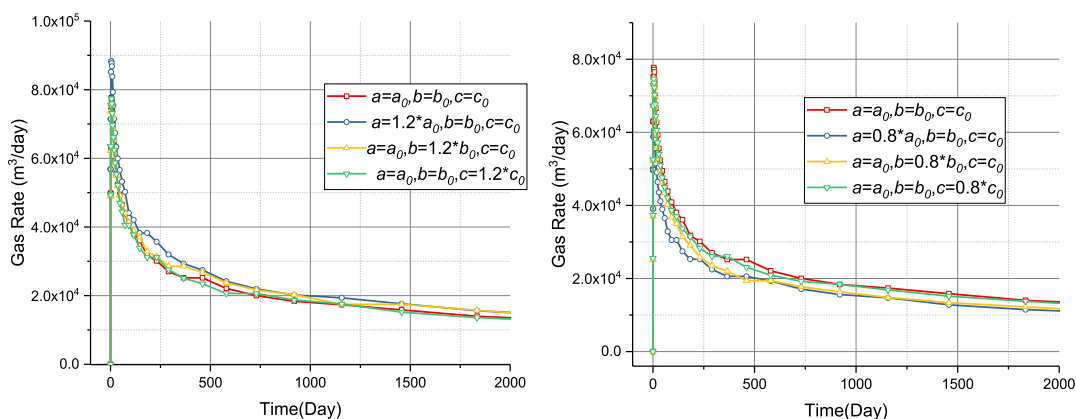


Figure 16. Production rate with (a) bigger axis lengths and (b) smaller axis lengths. *a*, *b*, and *c* separately refer to values of the *x*-, *y*-, and *z*-axes.

Table 3. Parameters of the Five Designed Cases^{37,63}

flow directions	parameters	case 1	case 2	case 3	case 4	case 5
X	k_{fx} (m ²)	4×10^{-18}	1×10^{-16}	2.5×10^{-16}	1×10^{-16}	2.5×10^{-16}
	c_{fx} (MPa ⁻¹)	0.078	0.0093	0.0030	0.0051	0.0083
Y	k_{fy} (m ²)	3.2×10^{-18}	8×10^{-17}	2×10^{-16}	1.1×10^{-16}	4×10^{-16}
	c_{fy} (MPa ⁻¹)	0.051	0.013	0.012	0.008	0.013
Z	k_{fz} (m ²)	1.6×10^{-19}	2×10^{-19}	5×10^{-18}	5×10^{-18}	1×10^{-17}
	c_{fz} (MPa ⁻¹)	0.03	0.01	0.01	0.009	0.013

the mass transfer between the fracture and the matrix systems determines the long-term gas production behavior.

4.4. Impacts of SRV Size. This section studies the effects of SRV size on shale gas production. Obviously, a larger SRV size would bring a higher production rate. However, in this work, the length of each axis is varied to investigate its impact on gas production. Figure 16 illustrates the gas production rate with different axis lengths.

It can be found from the figure that bigger axis values lead to larger gas rates whereas smaller axis values bring lower gas rates. The impacts of different axes' values on gas production behavior are quite different. The gas production rate is sensitive to the lengths of *x* and *y* axes as they bring the relative larger or smaller gas rates when the axis lengths are enhanced or decreased at the same ratio. Conversely, the variation of *z*-axis value has little impact on the shale gas production because of the lowest permeability value at the vertical direction. From the characteristics above, a conclusion can be drawn that the

SRV area should extend in the horizontal plane rather than the vertical direction.

4.5. Impacts of the Proppants. In the process of gas production, lots of proppants are injected into the reservoir to keep the fracture open during the gas production process. Evolution of fracture permeability behaviors differently with the varied proppant type and layer can be represented by the value of the permeability compressibility.⁶⁷ By performing a sequence of tests, Tan et al.^{37,63} investigated variations of permeability compressibility with different proppant type and layer. In this work, effects of proppant type and layer on shale gas production are studied by applying these values to our model. We designed five simulation cases as below and the details of these scenarios and parameters are illustrated in Table 3.

- Case 1: fractures with no proppants.
- Case 2: fractures supported by one layer of glass beads.
- Case 3: fractures supported by multilayer glass beads.
- Case 4: fractures supported by a single layer of sand.

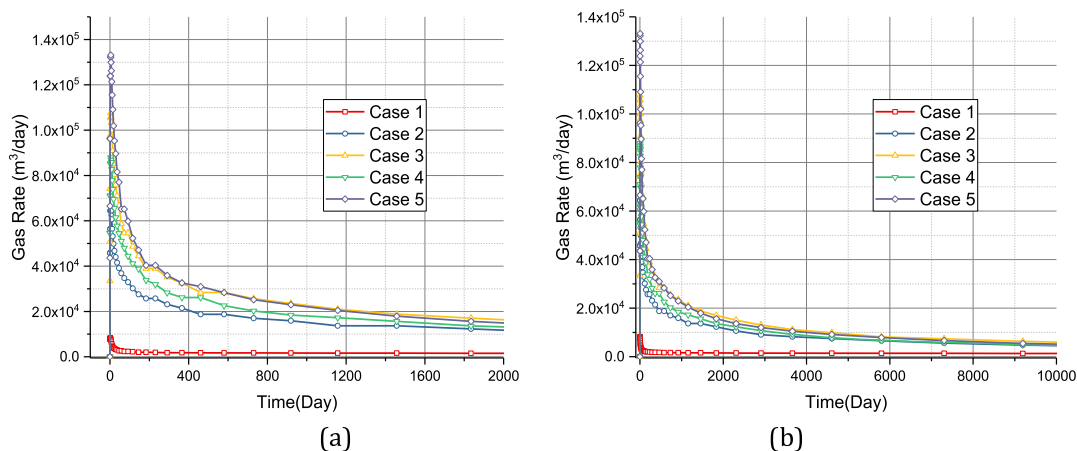


Figure 17. Impact of the proppant type and layer on the gas production behavior in a (a) short time and (b) long time.

Case 5: fractures supported by multilayer sand.

Production behavior of gas with different proppant type and layer are illustrated in Figure 17. Comparing Case 1 with other cases, we can find that the existence of the proppant substantially enhances production rates. Also, the gas rate behaves differently in different cases and the difference is lessened with the production time. Multiple layers of proppant bring a larger gas rate than that with one layer as shown in Figure 17. When comparing the efficiency of the proppant type, we find that for the one layer the sand is better than the glass, whereas for multiple layers the efficiencies of sand and glass are similar.

We also illustrated the permeability evolution and gas pressure variations with different cases in the gas depletion process (Figure 18). Here, the average value of the SRV region

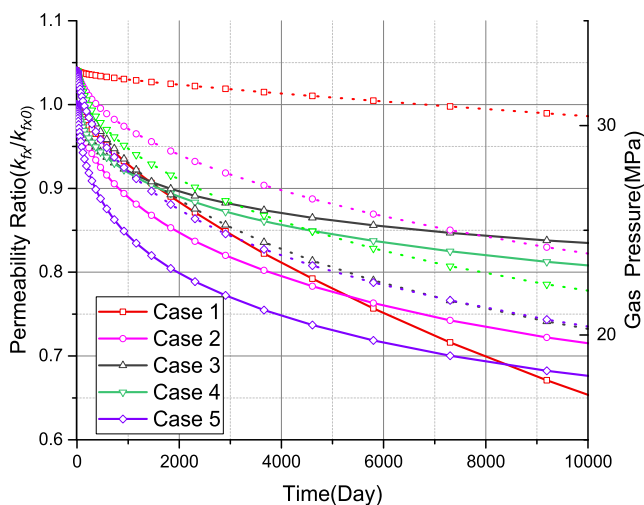


Figure 18. Permeability evolution and gas pressure variations with different proppant type and layer during the gas depletion process.

is illustrated. In the figure, the solid lines with different colors represent the permeability evolutions whereas the corresponding dot lines represent the gas pressure variations. The pressure drawdown of Case 1 (origin fracture with no proppants) is small and it has the largest permeability decrease gradient because of its largest permeability compressibility. Comparing Cases 2 and 3, and Cases 4 and 5, we find that the pressure drawdown with multiple layer proppants is larger than that

with one layer because of larger permeability. For the one-layer proppant, the sand (Case 4) has a larger permeability ratio than that with glass (Case 2) and it also brings a larger pressure drawdown. However, for the multiple-layer proppants, the sand (Case 5) has a smaller permeability ratio than that of glass (Case 3), whereas they brought a similar pressure drawdown. Comprehensively analyzing Figures 17 and 18, we find that Case 5 brings a larger initial gas rate compared with Case 3 because of its relative larger permeability value. Conversely, for the long-term gas flow rate, the value of multilayer sands (Case 5) is smaller than that of glass beads (Case 3) because of larger compressibility value.

4.6. Impacts of In Situ Stress. The permeability of shale is highly dependent on the effective stress. However, two cases of high effective stress usually occur in shale gas reservoir. The first is because of the high in situ stress which is often observed in deep shale reservoirs.⁶⁸ The second is gas depletion-induced effective stress increase.⁶⁹ As shown in this case, the initial gas pressure is up to 32.6 MPa whereas the bottom hole pressure is 3.69 MPa. The effective stress enhancement can be up to 30 MPa, especially near the wellbore or in the hydraulic fractures. The permeability evolution behaves differently under low and high effective stresses.⁶⁹ Under conditions with high effective stress, the fracture compressibility is not constant but depends on effective stress.⁵⁶ McKee et al.⁷⁰ introduced mean compressibility \bar{C}_f which decreased with increasing effective stress to replace C_f in eq 24

$$\bar{C}_f = \frac{C_{f0}}{\zeta(\sigma - \sigma_0)} (1 - e^{-\zeta(\sigma - \sigma_0)}) \quad (32)$$

where \bar{C}_f and C_{f0} represent the average compressibility value over stress interval $\sigma - \sigma_0$ and compressibility value under original effective stress σ_0 ; ζ denotes the decline rate for compressibility of pores with the rising effective stress.

Applying eq 32 into eq 24 yields

$$k_f = k_{f0} e^{-3C_{f0}/\zeta(\sigma - \sigma_0)(1 - e^{-\zeta(\sigma - \sigma_0)})} \quad (33)$$

Our recent research³⁹ successively measured the permeability for the nonpropped and propped fractures as effective stress increases to 59.5 from 1.5 MPa. Sand was used as proppant, and parameter fitting values of no proppant, monolayer, and multiple layers of proppants were obtained. This section investigated the effects of the high effective stress on permeability values, as well as gas production behavior with

these values. Also, three scenarios are designed to compare with the results in Section 4.4 and the parameters of the designed scenarios are illustrated in Table 4.³⁹ It should be

Table 4. Parameters of the Designed Scenarios under High Stress³⁹

parameter/description	case 1	case 4	case 5
	no proppants under high stress	one layer under high stress	multiple layers under high stress
k_{fx} (m ²)	4×10^{-18}	1×10^{-16}	2.5×10^{-16}
c_{fx0} (MPa ⁻¹)	0.103	0.023	0.025
ζ (MPa ⁻¹)	0.108	0.171	0.136

noted that only the permeability variation in the x -direction is measured in our recent research. Therefore, in this section only the value and variation of c_{fx} are different from those in Table 3, and the c_{fy} and c_{fz} are the same.

The impacts of stress on shale gas production are illustrated in Figure 19 and high stress brings a smaller gas rate. Comparing different cases, we find that the case with no proppants (Case 1) exhibits a huge difference under high stress, whereas the cases with one layer and multiple layers (Case 4 and Case 5) show little difference.

The permeability evolution and gas pressure variations with different stresses during the gas production process are shown in Figure 20. For Cases 4 and 5, the high stress brings a lower permeability value and the difference lessens with the increase of the proppant layer. The permeability ratio with one-layer proppant is larger than that with multiple layers for both stress lever because of its smaller pressure drawdown. For Case 1, the permeability value under high stress is larger than that with lower stress at the time scale as the gas pressure drawdown is smaller for the high-stress condition.

We also investigated the permeability evolutions with gas pressure under different cases and the results are shown in Figure 21. The permeability evolution with constant compressibility value exhibits an exponential decreasing trend without proppants (Case 1) but exhibits linear decreasing trend with proppants. Conversely, permeability evolutions with valuable compressibility value both exhibit an exponential decreasing trend with and without proppants. Comparing the behaviors under low stress and high stress, we can find that the

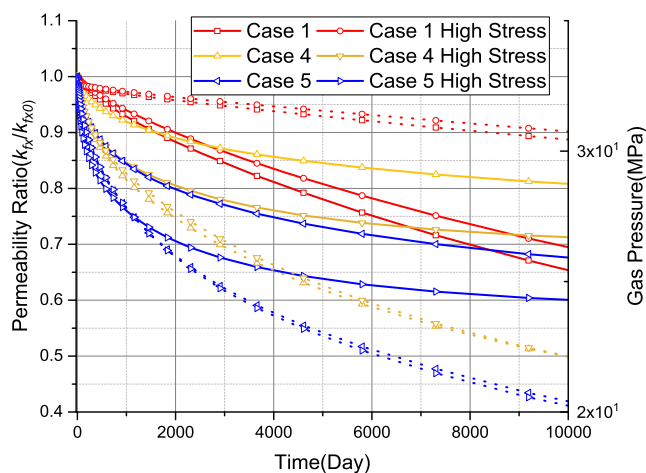


Figure 20. Permeability evolution and gas pressure variations with different effective stress levels during the gas depletion process.

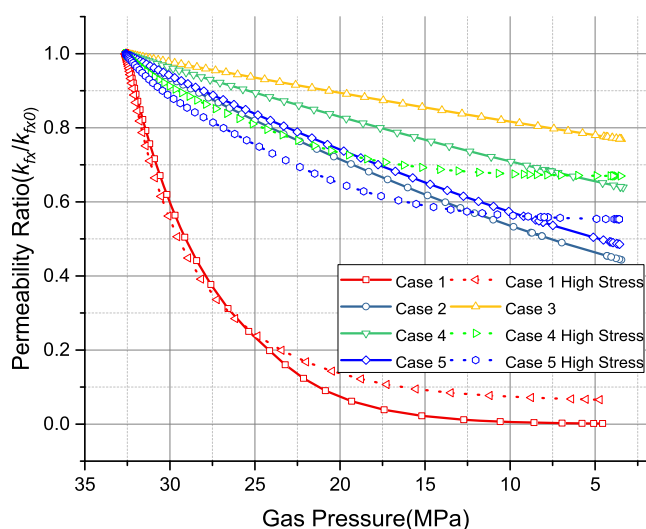


Figure 21. Permeability evolution with the gas pressure under different cases.

permeability value under high stress is first smaller than the value under low stress and becomes larger later.

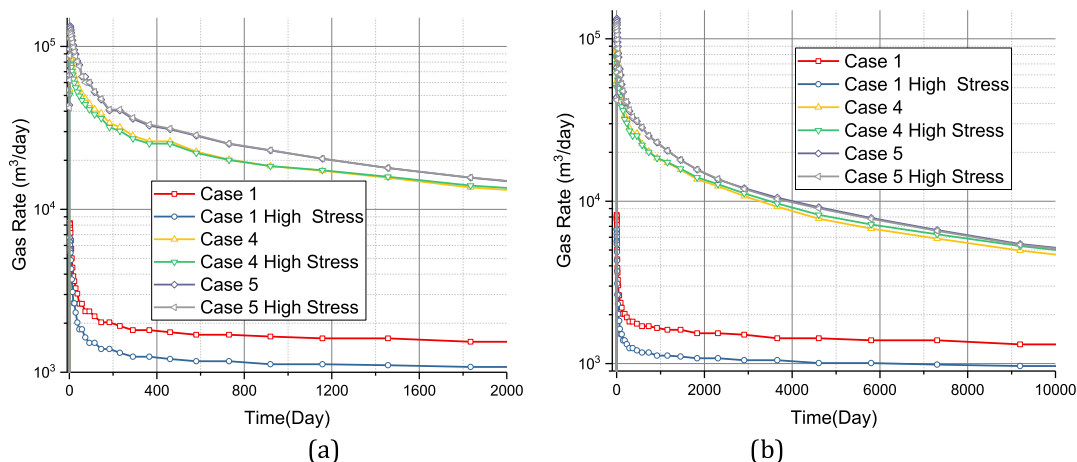


Figure 19. Impact of effective stress level on the gas production behavior in the (a) short term and (b) long term.

5. CONCLUSIONS

A multidomain multiscale model is proposed and applied to probe the impacts of HF-induced heterogeneity and complexity of response on shale gas production. Both an SRV and a USRV are included in the model with shapes and sizes determined from the evolution of the MS event cloud. Based on the results of the verified case and numerical simulations, we draw the following conclusions:

- 1 Two different simulation approaches can be established considering the different treatment methods of HF and the SRV is assumed ellipsoidal in shape instead of being artificially constrained to be rectangular. The impacts of variations of relative permeability and intrinsic permeability within the SRV are concentrated in early-time with gas rates in the long-term mainly dependent on the mass supply of free then adsorbed gas from the matrix system and then, at even later-times, the USRV region;
- 2 Key suggestions relate to the optimization of HF. The SRV region should be maximally expanded in the horizontal direction—to take advantage of the larger permeability in the horizontal plane. The permeability evolution function should be convex with respect to the distance and a concave response should be specifically avoided.
- 3 The value of the non-Darcy effect is much smaller than that in the coal reservoir because of its much smaller permeability. The distal transport of the proppant and its distribution remarkably enhances the gas production rate with multiple layers of proppant, generating a significantly larger gas rate than those resulting from merely a single layer. The stress-sensitivity of proppant permeability reduction to pressure drawdown decreases with an increase in the number of layers present in the proppant pack.
- 4 Specifically, for the selection of proppant type and placement, the resulting permeability and compressibility are of complementary importance as the first controls the initial gas flow rate whereas the second determines the permeability trend with time. The proposed model applies a new approach for optimizing the HF process and for analyzing the shale gas production behavior.

■ AUTHOR INFORMATION

Corresponding Authors

Yuling Tan — Key Laboratory of Tectonics and Petroleum Resources, Ministry of Education, China University of Geosciences, Wuhan 430074, China; orcid.org/0000-0001-9446-9069; Email: yulingtan@126.com

Tianyu Chen — Key Laboratory of Ministry of Education on Safe Mining of Deep Metal Mines, Northeastern University, Shenyang 110819, China; Email: chentianyu@mail.neu.edu.cn

Authors

Guanglei Cui — Key Laboratory of Ministry of Education on Safe Mining of Deep Metal Mines, Northeastern University, Shenyang 110819, China

Xia-Ting Feng — Key Laboratory of Ministry of Education on Safe Mining of Deep Metal Mines, Northeastern University, Shenyang 110819, China

Derek Elsworth — Department of Energy and Mineral Engineering, G3 Center and Energy Institute, The Pennsylvania State University, University Park PA16802, United States

Zhejun Pan — CSIRO Energy Business Unit, Clayton South 3169, Victoria, Australia; orcid.org/0000-0002-7292-630X

Chunguang Wang — State Key Laboratory of Mining Disaster Prevention and Control Co-founded by Shandong Province and the Ministry of Science and Technology, Shandong University of Science and Technology, Qingdao 266590, China

Complete contact information is available at:
<https://pubs.acs.org/10.1021/acs.energyfuels.0c00062>

Notes

The authors declare no competing financial interest.

■ ACKNOWLEDGMENTS

The research delivered partial results under supports of the China Postdoctoral Science Foundation (2019M661118), the Natural Science Foundation of China (51609038), the 111 Project (B17009), and the Fundamental Research Funds for the Central Universities (no. N160104002).

■ REFERENCES

- (1) Mayerhofer, M. J.; Lonon, E.; Warpinski, N. R.; Cipolla, C. L.; Walsler, D. W.; Rightmire, C. M. What Is Stimulated Reservoir Volume? *SPE Prod. Oper.* **2010**, *25*, 89–98.
- (2) Du, J.; Hu, L.; Meegoda, J. N.; Zhang, G. Shale softening: Observations, phenomenological behavior, and mechanisms. *Appl. Clay Sci.* **2018**, *161*, 290–300.
- (3) Fang, Y.; Elsworth, D.; Cladouhos, T. T. Reservoir permeability mapping using microearthquake data. *Geothermics* **2018**, *72*, 83–100.
- (4) Cipolla, C. L.; Fitzpatrick, T.; Williams, M. J.; Ganguly, U. K. Seismic-to-Simulation for Unconventional Reservoir Development. *SPE Reservoir Characterisation and Simulation Conference and Exhibition*; Society of Petroleum Engineers: Abu Dhabi, UAE, 2011; p 23.
- (5) Yu, X.; Rutledge, J.; Leaney, S.; Maxwell, S. Discrete-Fracture-Network Generation From Microseismic Data by Use of Moment-Tensor- and Event-Location-Constrained Hough Transforms. *SPE J.* **2016**, *21*, 221–232.
- (6) Williams-Stroud, S.; Ozgen, C.; Billingsley, R. L. Microseismicity-constrained discrete fracture network models for stimulated reservoir simulation. *Geophysics* **2013**, *78*, B37–B47.
- (7) Doe, T.; Shi, C.; Enachescu, C. Discrete Fracture Network Simulation of Production Data from Unconventional Wells. *SPE/AAPG/SEG Unconventional Resources Technology Conference*; Society of Petroleum Engineers: Denver, Colorado, USA, 2014.
- (8) Shakiba, M.; Cavalcante Filho, J. S. d. A.; Sepehrmoori, K. Using Embedded Discrete Fracture Model (EDFM) in numerical simulation of complex hydraulic fracture networks calibrated by microseismic monitoring data. *J. Nat. Gas Sci. Eng.* **2018**, *55*, 495–507.
- (9) Yong, Y. K.; Maulianda, B.; Wee, S. C.; Mohshim, D.; Elraies, K. A.; Wong, R. C.; Gates, I. D.; Eaton, D. Determination of stimulated reservoir volume and anisotropic permeability using analytical modelling of microseismic and hydraulic fracturing parameters. *J. Nat. Gas Sci. Eng.* **2018**, *58*, 234–240.
- (10) Cui, G.; Zhao, Y.; Liu, J.; Wei, M.; Elsworth, D. A Gaussian Decomposition Method and its applications to the prediction of shale gas production. *Fuel* **2018**, *224*, 331–347.
- (11) Yu, G.; Aguilera, R. 3D analytical modeling of hydraulic fracturing stimulated reservoir volume. *SPE Latin America and Caribbean Petroleum Engineering Conference*; Society of Petroleum Engineers, 2012.
- (12) Fisher, M. K.; Heinze, J. R.; Harris, C. D.; Davidson, B. M.; Wright, C. A.; Dunn, K. P. Optimizing Horizontal Completion

Techniques in the Barnett Shale Using Microseismic Fracture Mapping. *SPE Annual Technical Conference and Exhibition*; Society of Petroleum Engineers: Houston, Texas, 2004.

(13) Fan, D.; Ettehadtavakkol, A. Semi-analytical modeling of shale gas flow through fractal induced fracture networks with microseismic data. *Fuel* **2017**, *193*, 444–459.

(14) Rahimi Zeynal, A.; Snelling, P.; Neuhaus, C. W.; Mueller, M. Correlation of Stimulated Rock Volume from Microseismic Pointsets to Production Data—A Horn River Case Study. *SPE Western North American and Rocky Mountain Joint Meeting*; Society of Petroleum Engineers: Denver, Colorado, 2014.

(15) Wattenbarger, R. A.; El-Banbi, A. H.; Villegas, M. E.; Maggard, J. B. Production analysis of linear flow into fractured tight gas wells. *SPE Rocky Mountain Regional/Low-Permeability Reservoirs Symposium*; Colorado Society of Petroleum Engineers: Denver, 1998.

(16) Bello, R. O.; Wattenbarger, R. A. Modelling and analysis of shale gas production with a skin effect. *Canadian International Petroleum Conference*; Alberta Petroleum Society of Canada: Calgary, 2009.

(17) Al-Ahmadi, H. A.; Wattenbarger, R. A. Triple-porosity models: one further step towards capturing fractured reservoirs heterogeneity. *SPE/DGS Saudi Arabia Section Technical Symposium and Exhibition*; Society of Petroleum Engineers: Al-Khobar: Saudi Arabia, 2011.

(18) Stalgorova, K.; Mattar, L. Analytical model for unconventional multifractured composite systems. *SPE Reservoir Eval. Eng.* **2013**, *16*, 246–256.

(19) Zhang, F.; Emami-Meybodi, H. Flowback fracture closure of multi-fractured horizontal wells in shale gas reservoirs. *J. Pet. Sci. Eng.* **2020**, *186*, 106711.

(20) Roychaudhuri, B.; Tsotsis, T. T.; Jessen, K. An experimental investigation of spontaneous imbibition in gas shales. *J. Pet. Sci. Eng.* **2013**, *111*, 87–97.

(21) Guo, B.; Gao, D. The significance of fracture face matrix damage to the productivity of fractured wells in shale gas reservoirs. *Pet. Sci. Technol.* **2014**, *32*, 202–210.

(22) Chakraborty, N.; Karpyn, Z. T. Gas permeability evolution with soaking time in ultra tight shales. *SPE Annual Technical Conference and Exhibition*; Society of Petroleum Engineers: Houston, Texas, USA, 2015.

(23) Clarkson, C. R.; Williams-Kovacs, J. Modeling two-phase flowback of multifractured horizontal wells completed in shale. *SPE J.* **2013**, *18*, 795–812.

(24) Williams-Kovacs, J.; Clarkson, C. A Modified Approach For Modelling 2-Phase Flowback From Multi-Fractured Horizontal Shale Gas Wells. *Unconventional Resources Technology Conference*. San Antonio, Texas, USA, 2015.

(25) Yang, R.; Huang, Z.; Li, G.; Yu, W.; Sepehrnoori, K.; Tian, S.; Song, X.; Sheng, M. An innovative approach to model two-phase flowback of shale gas wells with complex fracture networks. *SPE Annual Technical Conference and Exhibition*; Society of Petroleum Engineers: Dubai, UAE, 2016.

(26) Jia, P.; Cheng, L.; Clarkson, C. R.; Williams-Kovacs, J. D. Flow behavior analysis of two-phase (gas/water) flowback and early-time production from hydraulically-fractured shale gas wells using a hybrid numerical/analytical model. *Int. J. Coal Geol.* **2017**, *182*, 14–31.

(27) Shang, X.; Wang, J.; Zhang, Z. Iterative Analytical Solutions for Nonlinear Two-phase Flow with Gas Solubility in Shale Gas Reservoirs. *Geofluids* **2019**, *2019*, 1–15.

(28) Wang, H.; Wang, J.; Gao, F.; Wang, X. A Two-phase Flowback Model for Multiscale Diffusion and Flow in Fractured Shale Gas Reservoirs. *Geofluids* **2018**, *2018*, 1–15.

(29) Yu, W.; Sepehrnoori, K. Simulation of gas desorption and geomechanics effects for unconventional gas reservoirs. *Fuel* **2014**, *116*, 455–464.

(30) Ren, L.; Su, Y.; Zhan, S.; Meng, F.; Zhao, G. Fully coupled fluid-solid numerical simulation of stimulated reservoir volume (SRV)-fractured horizontal well with multi-porosity media in tight oil reservoirs. *J. Pet. Sci. Eng.* **2019**, *174*, 757–775.

(31) Wang, H.; Wang, J. G.; Gao, F.; Wang, X. A Two-Phase Flowback Model for Multiscale Diffusion and Flow in Fractured Shale Gas Reservoirs. *Geofluids* **2018**, *2018*, 1–15.

(32) Patterson, R.; Yu, W.; Wu, K. Integration of microseismic data, completion data, and production data to characterize fracture geometry in the Permian Basin. *J. Nat. Gas Sci. Eng.* **2018**, *56*, 62–71.

(33) Shao, Y.; Huang, X.; Xing, Y. An integrated study on the sensitivity and uncertainty associated with the evaluation of stimulated reservoir volume (SRV). *J. Pet. Sci. Eng.* **2017**, *159*, 903–914.

(34) Zhang, F.; Mack, M. Integrating fully coupled geomechanical modeling with microseismicity for the analysis of refracturing treatment. *J. Nat. Gas Sci. Eng.* **2017**, *46*, 16–25.

(35) Shapiro, S.; Huenges, E.; Borm, G. Estimating the crust permeability from fluid-injection-induced seismic emission at the KTB site. *Geophys. J. Int.* **1997**, *131*, 15–18.

(36) Yu, G.; Aguilera, R. 3D Analytical Modeling of Hydraulic Fracturing Stimulated Reservoir Volume. *SPE Latin America and Caribbean Petroleum Engineering Conference*; Society of Petroleum Engineers: Mexico City, Mexico, 2012.

(37) Tan, Y.; Pan, Z.; Liu, J.; Feng, X.-T.; Connell, L. D. Laboratory study of proppant on shale fracture permeability and compressibility. *Fuel* **2018**, *222*, 83–97.

(38) Wang, J.; Elsworth, D. Role of proppant distribution on the evolution of hydraulic fracture conductivity. *J. Pet. Sci. Eng.* **2018**, *166*, 249–262.

(39) Chen, T.; Feng, X.-T.; Tan, Y.; Cui, G.; Pan, Z. Gas permeability and fracture compressibility for proppant-supported shale fractures under high stress. *J. Pet. Sci. Eng.*, **2020**; under review.

(40) Ambrose, R. J.; Hartman, R. C.; Campos, M. D.; Akkutlu, I. Y.; Sondergeld, C. New Pore-scale Considerations for Shale Gas in Place Calculations. *SPE Unconventional Gas Conference*; Society of Petroleum Engineers: Pittsburgh, Pennsylvania, USA, 2010.

(41) Wang, J. G.; Kabir, A.; Liu, J.; Chen, Z. Effects of non-Darcy flow on the performance of coal seam gas wells. *Int. J. Coal Geol.* **2012**, *93*, 62–74.

(42) Cui, G.; Liu, J.; Wei, M.; Feng, X.; Elsworth, D. Evolution of permeability during the process of shale gas extraction. *J. Nat. Gas Sci. Eng.* **2018**, *49*, 94–109.

(43) Cui, G.; Xia-Ting, F.; Pan, Z.; Chen, T.; Liu, J.; Elsworth, D.; Tan, Y.; Wang, C. Impact of shale matrix mechanical interactions on gas transport during production. *J. Pet. Sci. Eng.* **2020**, *184*, 106524.

(44) Cao, P.; Liu, J.; Leong, Y.-K. A multiscale-multiphase simulation model for the evaluation of shale gas recovery coupled the effect of water flowback. *Fuel* **2017**, *199*, 191–205.

(45) Ma, T.; Rutqvist, J.; Oldenburg, C. M.; Liu, W.; Chen, J. Fully coupled two-phase flow and poromechanics modeling of coalbed methane recovery: Impact of geomechanics on production rate. *J. Nat. Gas Sci. Eng.* **2017**, *45*, 474–486.

(46) Ye, Z.; Chen, D.; Wang, J. G. Evaluation of the non-Darcy effect in coalbed methane production. *Fuel* **2014**, *121*, 1–10.

(47) Cooke, C. E., Jr. Conductivity of Fracture Proppants in Multiple Layers. *J. Pet. Technol.* **1973**, *25*, 1101–1107.

(48) Wei, Z.; Zhang, D. A fully coupled multiphase multicomponent flow and geomechanics model for enhanced coalbed-methane recovery and CO₂ storage. *SPE J.* **2013**, *18*, 448–467.

(49) Sun, Z.; Shi, J.; Wu, K.; Miao, Y.; Zhang, T.; Feng, D.; Xiao, Z.; Wu, N.; Lin, W.; Li, X. A fully-coupled gas-water two phase productivity equations for low-permeability CBM wells. *J. Pet. Sci. Eng.* **2018**, *166*, 611–620.

(50) Brooks, R. H.; Corey, A. T. Hydraulic properties of porous media and their relation to drainage design. *Trans. ASAE* **1964**, *7*, 0026–0028.

(51) Leverett, M. C. Capillary behavior in porous solids. *Trans. ASAE* **1941**, *142*, 152–169.

(52) Chen, Y.; Ma, G.; Wang, H.; Li, T.; Wang, Y. Application of carbon dioxide as working fluid in geothermal development considering a complex fractured system. *Energy Convers. Manage.* **2019**, *180*, 1055–1067.

(53) Cui, G.; Liu, J.; Wei, M.; Shi, R.; Elsworth, D. Why shale permeability changes under variable effective stresses: New insights. *Fuel* **2018**, *213*, 55–71.

(54) Javadpour, F. Nanopores and Apparent Permeability of Gas Flow in Mudrocks (Shales and Siltstone). *J. Can. Petrol. Technol.* **2009**, *48*, 16–21.

(55) Chen, Y. D.; Yang, R. T. Concentration dependence of surface diffusion and zeolitic diffusion. *AIChE J.* **1991**, *37*, 1579–1582.

(56) Chen, D.; Pan, Z.; Ye, Z. Dependence of gas shale fracture permeability on effective stress and reservoir pressure: Model match and insights. *Fuel* **2015**, *139*, 383–392.

(57) Al-Ahmadi, H. A.; Wattenbarger, R. A. Triple-porosity Models: One Further Step Towards Capturing Fractured Reservoirs Heterogeneity. *SPE/DGS Saudi Arabia Section Technical Symposium and Exhibition*; Society of Petroleum Engineers: Al-Khobar: Saudi Arabia, 2011.

(58) Meyer, B. R.; Bazan, L. W.; Jacot, R. H.; Lattibeaudiere, M. G. Optimization of Multiple Transverse Hydraulic Fractures in Horizontal Wellbores. *SPE Unconventional Gas Conference*; Society of Petroleum Engineers: Pittsburgh, Pennsylvania, USA, 2010.

(59) Martineau, D. F. History of the Newark East Field and the Barnett Shale as a gas reservoir. *AAPG Bull.* **2007**, *91*, 399–403.

(60) Yu, W.; Zhang, T.; Du, S.; Sepehrnoori, K. Numerical study of the effect of uneven proppant distribution between multiple fractures on shale gas well performance. *Fuel* **2015**, *142*, 189–198.

(61) Cao, P.; Liu, J.; Leong, Y.-K. A fully coupled multiscale shale deformation-gas transport model for the evaluation of shale gas extraction. *Fuel* **2016**, *178*, 103–117.

(62) Lee, D. S.; Herman, J. D.; Elsworth, D.; Kim, H. T.; Lee, H. S. A critical evaluation of unconventional gas recovery from the marcellus shale, northeastern United States. *KSCE J. Civ. Eng.* **2011**, *15*, 679.

(63) Tan, Y.; Pan, Z.; Liu, J.; Wu, Y.; Haque, A.; Connell, L. D. Experimental study of permeability and its anisotropy for shale fracture supported with proppant. *J. Nat. Gas Sci. Eng.* **2017**, *44*, 250–264.

(64) Ishida, T.; Chen, Y.; Bennour, Z.; Yamashita, H.; Inui, S.; Nagaya, Y.; Naoi, M.; Chen, Q.; Nakayama, Y.; Nagano, Y. Features of CO₂ fracturing deduced from acoustic emission and microscopy in laboratory experiments. *J. Geophys. Res.: Solid Earth* **2016**, *121*, 8080–8098.

(65) Gan, Q.; Elsworth, D.; Alpern, J. S.; Marone, C.; Connolly, P. Breakdown pressures due to infiltration and exclusion in finite length boreholes. *J. Pet. Sci. Eng.* **2015**, *127*, 329–337.

(66) Jia, Y.; Lu, Y.; Elsworth, D.; Fang, Y.; Tang, J. Surface characteristics and permeability enhancement of shale fractures due to water and supercritical carbon dioxide fracturing. *J. Pet. Sci. Eng.* **2018**, *165*, 284–297.

(67) Tan, Y.; Pan, Z.; Feng, X.-T.; Zhang, D.; Connell, L. D.; Li, S. Laboratory characterisation of fracture compressibility for coal and shale gas reservoir rocks: A review. *Int. J. Coal Geol.* **2019**, *204*, 1–17.

(68) Gutierrez, M.; Katsuki, D.; Tutuncu, A. Determination of the continuous stress-dependent permeability, compressibility and poroelasticity of shale. *Mar. Pet. Geol.* **2015**, *68*, 614–628.

(69) Chen, T.; Feng, X.-T.; Cui, G.; Tan, Y.; Pan, Z. Experimental study of permeability change of organic-rich gas shales under high effective stress. *J. Nat. Gas Sci. Eng.* **2019**, *64*, 1–14.

(70) McKee, C. R.; Bumb, A. C.; Koenig, R. A. Stress-Dependent Permeability and Porosity of Coal and Other Geologic Formations. *SPE Form. Eval.* **1988**, *3*, 81–91.